Carbonic Anhydrase Inhibition Sensitizes Group 3 Medulloblastoma to Radiotherapy

Cory M. Richman[1,2,3], Alexandra Rasnitsyn[1,2,3], Borja L. Holgado[1,2], Maria Vladoiu[1,2], Namal Abeysundara[1,2], Sandra Majo[4], Sara Chabi[4], Lucie J. Taunay[4], Hiromichi Suzuki[5], Ichiyo Shibahara[6], Joonas Haapasalo[1,2,7], Jonelle G. Pallotta[1,2], Tajana Douglas[1,2], Kaitlin Kharas[1,2,8], Kyle Juraschka[1,2,8,9], Oliver Ocsenas[3,10], Sachin A. Kumar[1,2,8], Kristiina Nordfors[1,2,11], Ana Guerreiro Stücklin[1,2,12], Raul A. Suarez[1,2], Jiao Zhang[13,14], Xiaochong Wu[13,14], Craig Daniels[13,14], Livia Garzia[15], Jüri Reimand[3,10,16], Olivier Saulnier[1,2,17], Thomas E. Merchant[18], Celio Pouponnot[4], David R. Raleigh[19,20,21], Michael D. Taylor[1,2,3,8,13,14,22,23,24], and Pasqualino De Antonellis[1,2,25]

ABSTRACT

Group 3 (G3) medulloblastoma constitutes the most aggressive molecular subgroup, and nearly all patients present with metastases upon recurrence. Treatment for newly diagnosed medulloblastoma relies on a combination of maximal safe surgical resection, followed by chemotherapy and ionizing radiation, and no therapies have been shown to confer a survival benefit at the time of recurrence. Given the limited therapeutic options available for patients with medulloblastoma, especially at recurrence, and the incomplete understanding of the molecular mechanisms underlying resistance to treatment, we sought to uncover actionable targets and biomarkers that could help refine patient selection and treatment of newly diagnosed medulloblastoma to reduce the risk of recurrence. In clinically relevant mouse models of G3 medulloblastoma, CT-guided fractionated radiotherapy extended overall survival and induced the clonal selection of radioresistant subpopulations of tumor cells that drove medulloblastoma recurrence. Comparison of recurrent tumors with treatment-naïve newly diagnosed tumors revealed a gene expression signature that was found to be a biomarker of radioresistance and poor prognosis. This prognostic gene signature was shown to be subgroup specific in a large patient cohort. Recurrent tumors had elevated expression of carbonic anhydrase 4, and genetic and pharmacologic modulation of carbonic anhydrase 4 could promote or reduce resistance to radiotherapy. These data suggest that the FDA-approved carbonic anhydrase inhibitor acetazolamide may be a useful radiosensitizer to improve the efficacy of the treatment of newly diagnosed G3 medulloblastoma that could reduce the risk of tumor recurrence and improve survival in pediatric patients.

Significance: G3 medulloblastoma features a prognostic subgroup-specific gene expression signature and can be targeted with a carbonic anhydrase inhibitor to enhance radiosensitivity, reducing the risk of recurrence and improving survival.

[1]The Arthur and Sonia Labatt Brain Tumour Research Centre, The Hospital for Sick Children, Toronto, Canada. [2]Developmental & Stem Cell Biology Program, The Hospital for Sick Children, Toronto, Canada. [3]Department of Medical Biophysics, University of Toronto, Toronto, Canada. [4]Institut Curie, CNRS UMR3347, INSERM U1021, University UPSaclay, PSL, Equipe Labellisée Ligue Contre le Cancer, Centre Universitaire, Orsay, France. [5]Division of Brain Tumor Translational Research, National Cancer Center Research Institute, Tokyo, Japan. [6]Department of Neurosurgery, Kitasato University School of Medicine, Sagamihara, Japan. [7]Center for Child, Adolescent and Maternal Health Research, Faculty of Medicine and Health Technology, Department of Neurosurgery, Tampere University Hospital, Wellbeing Services of Pirkanmaa, Tampere University, Tampere, Finland. [8]Department of Laboratory Medicine and Pathology, University of Toronto, Toronto, Canada. [9]Department of Neurosurgery, The Hospital for Sick Children, Toronto, Canada. [10]Computational Biology Program, Ontario Institute for Cancer Research, Toronto, Canada. [11]Center for Child, Adolescent and Maternal Health Research, Faculty of Medicine and Health Technology, Department of Pediatrics, Tampere University Hospital, Wellbeing Services of Pirkanmaa, Tampere University, Tampere, Finland. [12]Translational Brain Tumor Research Group, Children's Research Center, University Children's Hospital Zurich, Zurich, Switzerland. [13]Texas Children's Cancer and Hematology Center, Houston, Texas. [14]Department of Pediatrics – Hematology/Oncology, Baylor College of Medicine, Houston, Texas. [15]Cancer Research Program, McGill University Health Centre Research Institute, Montreal, Canada. [16]Department of Molecular Genetics, University of Toronto, Toronto, Canada. [17]Inserm U1330, Genomics and Development of Childhood Cancers Lab, Institut Curie, PSL University, SIREDO Oncology Center, Paris, France. [18]Department of Radiation Oncology, St. Jude Children's Research Hospital, Memphis, Tennessee. [19]Department of Radiation Oncology, University of California San Francisco, San Francisco, California. [20]Department of Neurological Surgery, University of California San Francisco, San Francisco, California. [21]Department of Pathology, University of California San Francisco, San Francisco, California. [22]Department of Neurosurgery, Baylor College of Medicine, Houston, Texas. [23]Department of Neurosurgery, Texas Children's Hospital, Houston, Texas. [24]Dan L Duncan Comprehensive Cancer Center, Baylor College of Medicine, Houston, Texas. [25]Dipartimento di Medicina Molecolare e Biotecnologie Mediche (DMMBM)'Federico II' University of Naples, Naples, Italy.

Corresponding Authors: Michael D. Taylor, Baylor College of Medicine, 1102 Bates Avenue, Feigin Tower, 10th Floor, Houston, TX 77030. E-mail: mdt.cns@gmail.com; and Pasqualino De Antonellis, Dipartimento di Medicina Molecolare e Biotecnologie Mediche (DMMBM)'Federico II' University of Naples, Naples 80145, Italy. E-mail: pasqualino.deantonellis@unina.it

Cancer Res 2025;85:3737–51

doi: 10.1158/0008-5472.CAN-24-3894

Introduction

Medulloblastoma is a devastating cancer of the cerebellum that constitutes 20% of all primary central nervous system tumors in children. Recent integrative genomic, transcriptomic, and DNA methylation profiling have stratified medulloblastoma into four consensus molecular subgroups: wingless, sonic-hedgehog, group 3 (G3), and group 4 (G4; ref. 1). G3 and G4 subgroup medulloblastomas account for approximately 60% of patient diagnoses and remain the least understood with respect to their pathogenesis and developmental origins. Most patients with G3 medulloblastoma develop metastases at the time of tumor recurrence, and relapsed tumors exhibit cellular heterogeneity that is distinct from therapy-naïve medulloblastoma (2). More broadly, G3 is the most aggressive molecular subgroup of medulloblastoma and has a high potential for metastatic spread that is responsible for most patient deaths (3).

Current therapy for medulloblastoma typically involves a combination of surgery, multi-agent chemotherapy, and craniospinal irradiation (CSI). However, in particularly young children in whom radiotherapy (RT) can cause devastating neurocognitive sequelae, CSI may be omitted in favor of tandem transplant (4, 5). There is currently no standard of care for patients with relapsed medulloblastoma, which is frequently lethal (6, 7). Treatment failure and relapse occur in up to one third of patients and confer an abysmal prognosis, with less than 10% of patients surviving 5 years after relapse (8, 9).

Here, we use a combination of human samples, preclinical models, bioinformatics, and mechanistic and functional approaches to define pathways that drive G3 medulloblastoma recurrence after CSI to shed light on therapeutic vulnerabilities that may enhance the efficacy of treatment. Using a fractionated CSI protocol resembling the standard clinical regimen for patients, we found that G3 medulloblastoma recurrences were transcriptionally distinct from primary tumors and leveraged this finding to derive a subgroup-specific radiation resistance gene expression signature. We show that carbonic anhydrase 4 (CA4) is sufficient to drive G3 medulloblastoma radioresistance and represents a druggable dependency whereby pharmacologic inhibition with acetazolamide (ACTZ) significantly improves survival in preclinical models. Given that ACTZ is a blood–brain barrier–permeable FDA-approved drug with an excellent safety profile in children and adults, these findings suggest that CA4 inhibition could improve survival for children with G3 medulloblastoma by sensitizing tumors to RT and reducing the risk of recurrence.

Materials and Methods

Patient-derived xenografts and cell lines

All samples used in this study were obtained with the written informed consent of patients, and all experimental procedures were performed in accordance with the Research Ethics Boards at The Hospital for Sick Children (Toronto, Canada, protocol REB1000024587). MB002SU (RRID: CVCL_VU79) and D425-Med (RRID: CVCL_1275) were kindly provided by Robert Wechsler-Reya's lab in 2016, Sanford Burnham Prebys, Medical Discovery Institute, La Jolla, CA. The patient-derived xenograft (PDX) lines Med-411FH, Med-211FH, and Med-114FH were generated by Jim Olson's lab and obtained in 2016, Fred Hutchinson Cancer Research Center, Seattle, WA (10). All cell lines originated from G3 medulloblastoma tissues with the following characteristics: Med-114FH from a 6.6-year-old female with *MYC*-amplified anaplastic large cell medulloblastoma; Med-411FH from a 3-year-old male with *MYC*-amplified, isochromosome 17 anaplastic large cell medulloblastoma; Med-211FH from a 2.8-year-old male with *MYC*-amplified, *GFI1B*-activated, *KRAS*-mutated medulloblastoma; MB002SU from a young male with metastatic, treatment-refractory (chemotherapy only) *MYC*-amplified medulloblastoma (11); and D425-Med from a 6-year-old male with *MYC*-amplified, *P53*-mutated medulloblastoma. The identity of each cell line was validated by short tandem repeat profiling (GenePrint, Promega). Cell lines were cultured in serum-free expansion media composed of Neurobasal medium (Gibco, 21103049) supplemented with 10 ng/mL EGF (Sigma-Aldrich, E9644), 10 ng/mL bFGF (PeproTech, 100-18B), 1X B27 (Thermo Fisher Scientific, 12587-010), 1X N2 (Thermo Fisher Scientific, 17502-048), 1X GlutaMAX (Thermo Fisher Scientific, 35050061), 75 μg/mL BSA (Sigma-Aldrich, A84l2), and 2 μg/mL heparin (Sigma-Aldrich, H3393). All cell lines used in the study were tested and confirmed to be negative for *Mycoplasma* contamination before use in experimental settings. PDXs were exclusively propagated orthotopically in NOD rag gamma (RRID: IMSR_JAX:007799) mice for less than five passages and kept in culture for the minimal time required to infect with luciferase and fluorescent reporters via lentivirus. Cell line expression of CA4 was assessed via Western blotting (R&D Systems, cat. #AF2186, RRID: AB_2290552), with GAPDH used as a housekeeping control (Abcam, cat. #ab9485, RRID: AB_307275).

Production of plasmids and viral supernatant

To generate lentiviral particles, human embryonic kidney HEK293T cells (RRID: CVCL_0045) were cotransfected with the pBMN (CMV-copGFP-Luc2-Puro) plasmid and second-generation lentiviral packaging plasmids pMD2.G VSVG and psPAX2. The supernatant containing lentiviral particles was collected 72 hours after transfection and concentrated using the Lenti-X concentrator (Clontech, 631231). Titration was carried out for each PDX/cell line to ensure a multiplicity of infection of 0.3 as previously described (12). Plasmids were obtained from Addgene, with pBMN (CMV-copGFP-Luc2-Puro) gifted from M. Essand (RRID: Addgene_80389) and pMD2.G and psPAX2 gifted from D. Trono (RRID: Addgene_12259 and RRID: Addgene_12260, respectively).

The overexpression of CA4 was induced using a construct [pLV(Exp)-mCherry:T2A:Bsd-CMV>h*CA4*(NM_000717.3), vector ID: VB180629-1145fah] from VectorBuilder, which was subsequently modified through site-directed mutagenesis to express the enzymatically defective CA4 isoform (R219S).

Orthotopic injection of tumor cells and bioluminescent imaging

Medulloblastoma PDXs were stereotactically engrafted using 20,000 cells in 3 μL total volume into the cerebellum of 6-week-old NOD rag gamma immunodeficient mice using the following coordinates: 2 mm posterior from lambda, 1 mm lateral, 3 mm deep, and 1 mm retraction to inject at a final depth of 2 mm as previously described (12). Xenografted mice underwent weekly bioluminescence through the administration of intraperitoneal injections using 150 mg/kg D-luciferin (PerkinElmer, 122796) under anesthesia using 2.5% isoflurane gas. Imaging was conducted 5 minutes after injection using a Xenogen Spectrum (IVIS-Spectrum) imaging system and analyzed using Living Image Software (PerkinElmer).

Mice received fractionated CSI once a baseline bioluminescent tumor signal of 1×10^6 photons per second was reached. RT was administered using an image-guided small-animal irradiator (X-Rad225CX, Precision X-Ray). Fractionated delivery was performed using two parallel opposed-lateral beams to account for

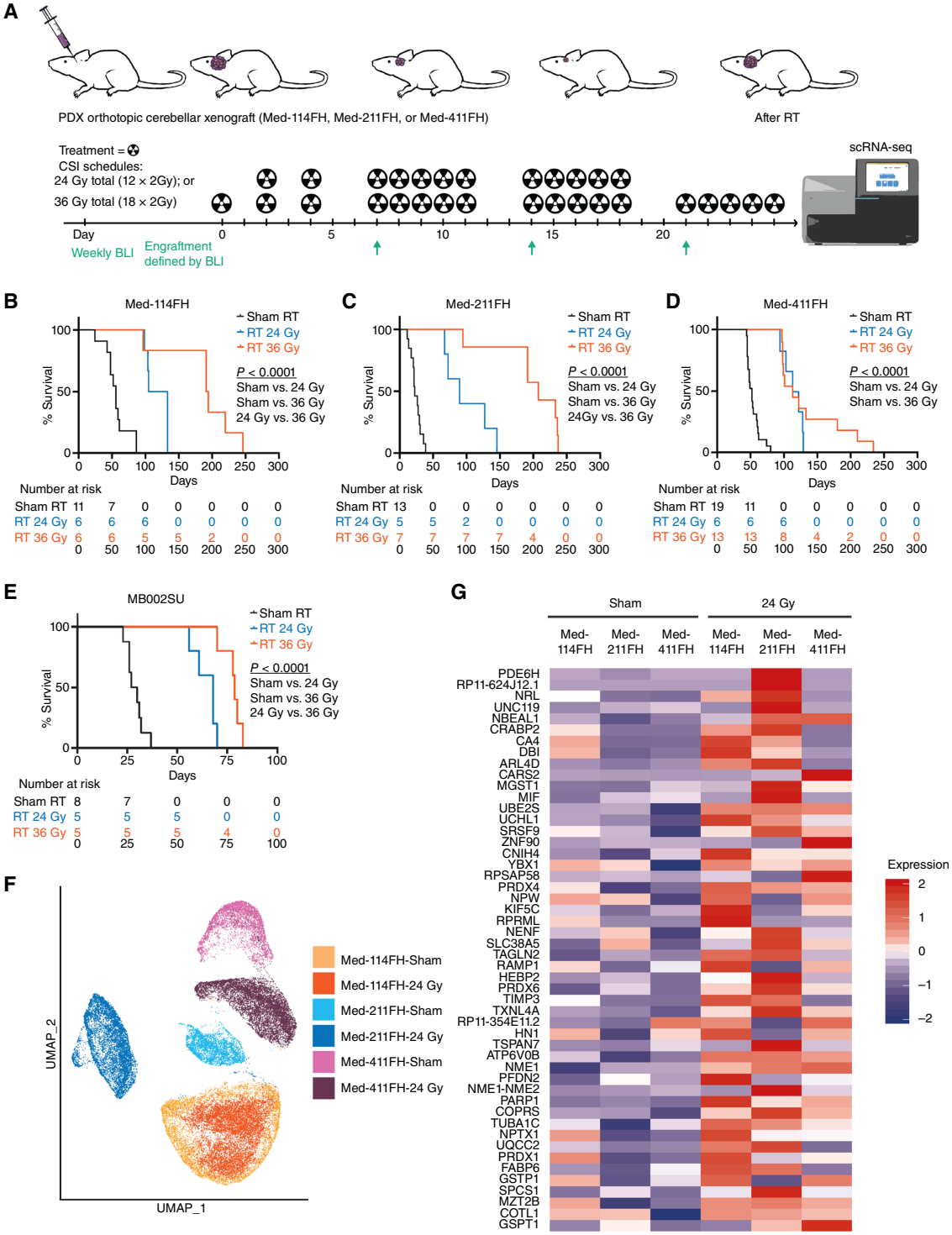

Figure 1.

Modeling radiation resistance in G3 medulloblastoma. **A,** Schematic depicting the protocol for CSI prescribing 24 Gy or 36 Gy at 2 Gy per fraction in mice engrafted with G3 medulloblastoma PDXs. **B–E,** Kaplan–Meier survival curves for control sham- (black), 24 Gy (blue)–, and 36 Gy (red)–irradiated mice engrafted with GFP-luciferase–tagged Med-114FH, Med-211FH, and Med-411FH PDXs. MB002SU was used to assess efficacy in a treatment-refractory tumor. Comparisons of survival among treated (36 Gy and 24 Gy) and sham groups were performed using log-rank (Mantel–Cox) tests. The number of mice per group (*n*) is indicated below each graph. Significance levels are represented as $P < 0.0001$. **F,** Uniform Manifold Approximation and Projection (UMAP) of single-cell expression data from sham- and 24 Gy–irradiated PDX tumors Med-114FH, Med-211FH, and Med-411FH. Object consists of greater than 50,000 cells harvested from six mice per replicate. **G,** Heatmap depicting the top 50 commonly differentially expressed genes when comparing sham- to 24 Gy–irradiated PDXs.

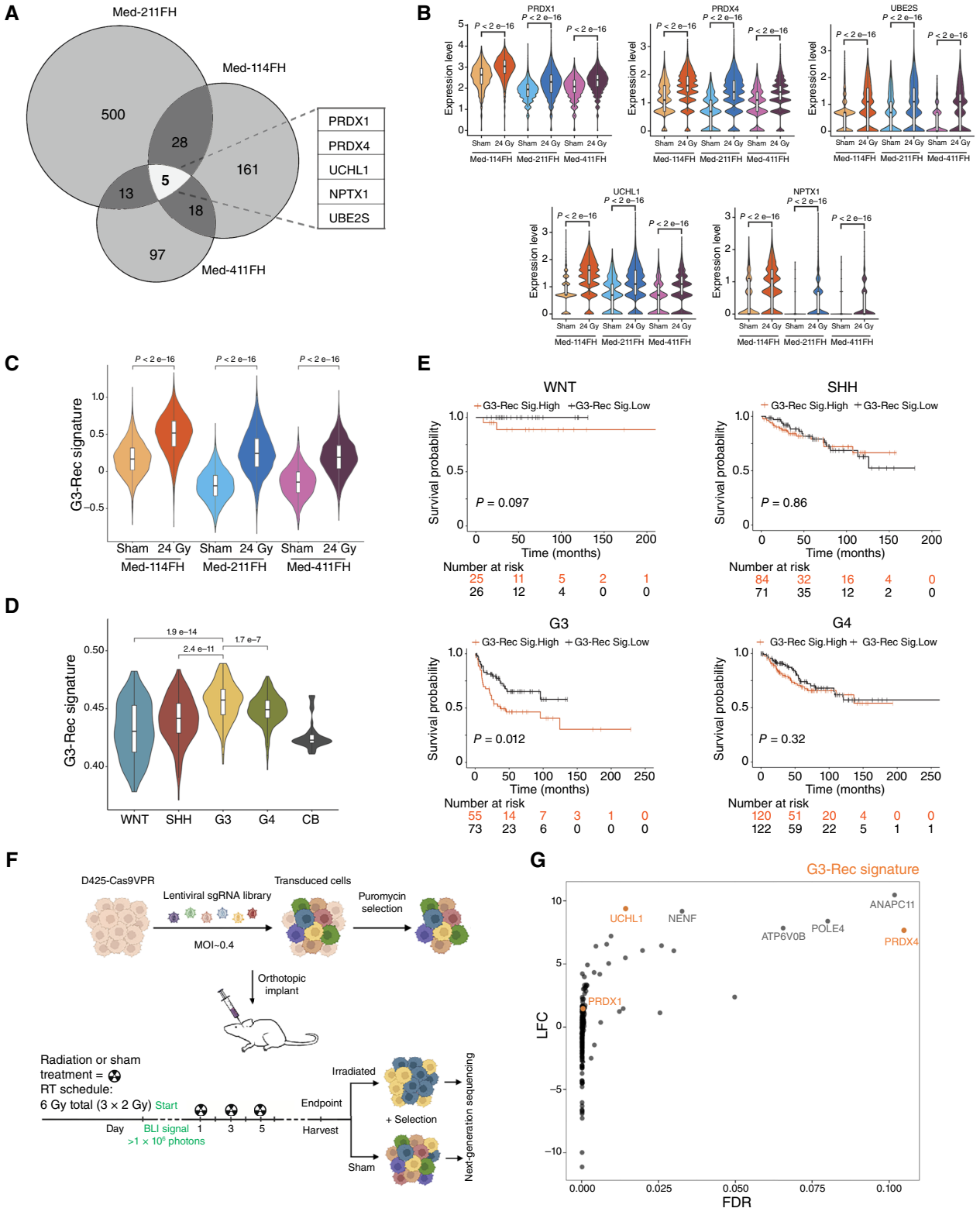

Figure 2.

Derivation of a G3-specific recurrent transcriptional signature. **A,** Venn diagram depicting the overlap of genes significantly upregulated in the 24 Gy–treated recurrent tumors of mice implanted with Med-114FH, Med-211FH, and Med-411FH. The five overlapping genes that constitute a G3 recurrent signature are listed. **B,** Violin plots depicting the normalized gene expression of *PRDX1, PRDX4, UBE2S, UCHL1*, and *NPTX1* across the different (*Continued on the following page.*)

tissue attenuation. The imaging approach involved a volumetric three-dimensional CT-guided approach for precise targeting of the brain and/or spinal cord as indicated in corresponding figure legends. Detailed methodology has been reported previously by Morrissy and colleagues (13). Tumors were monitored and left until predefined neurologic symptoms appeared or humane endpoint was reached. Clinical endpoints were evaluated by veterinary technicians blinded to experimental groups. The survival of mice was determined using Kaplan–Meier curves with differences between conditions evaluated using log-rank (Mantel–Cox) testing with GraphPad Prism (RRID: SCR_002798). Mice without a brain tumor at endpoint were censored and depicted with a dash on all associated survival curves. All animal work was approved by the Toronto Centre for Phenogenomics (RRID: SCR_006143) and STTARR Animal Care Committee (AUP 4524), and our study complied with all relevant ethical regulations. ACTZ, methazolamide (METHA), and polyethylene glycol vehicle were administered through intraperitoneal injection at 50 mg/kg twice daily. Analysis of bioluminescence was conducted by assessing the fold change in photons throughout the course of treatment relative to baseline (day 0, 0 Gy).

Tissue handling and dissociation

Fresh tumor tissues were resected under a stereoscope at endpoint. PDX tumor tissues were mechanically and enzymatically dissociated using a collagenase-based dissociation method as previously reported (14), followed by immediate single-cell dissociation as described below.

Single-cell RNA sequencing

Reverse transcription, amplification, and sequencing

Approximately 10,000 to 16,000 tissue-dissociated viable cells were loaded per sample on the Chromium Controller for encapsulation into gel beads-in-emulsion for reverse transcription of barcoded RNA. This was followed by Dynabead clean-up, PCR amplification, and solid-phase reversible immobilization (SPRI)–select bead clean-up using the Chromium Single Cell 3′ Gel Bead kit. Indexed single-cell libraries were generated using the Chromium Single Cell 3′ Library kit and the Chromium i7 Multiplex kit. Each 10× library was subjected to quality control using the Agilent 2100 Bioanalyzer system and sequenced using the Illumina sequencing platform by The Centre for Applied Genomics (RRID: SCR_001840).

Alignment of raw reads with 10X CellRanger's pipeline

BCL files were demultiplexed into FASTQ files and aligned to the reference human genome GRCh38 (hg38) to generate raw gene–barcode count matrices. When clustering multiple samples, CellRanger aggregation was performed to account for sequencing depth variation, followed by quality control and normalization metrics before re-computing the gene–barcode matrices. Human single-cell datasets were normalized using methods derived from the Scran pipeline and size factors were calculated and applied to normalize gene expression, generating normalized log expression values for each dataset (RRID: SCR_016944).

Clustering and visualization

Clustering analysis was performed with both the presence and absence of cell cycle–related genes obtained from Ensembl BioMart. When implemented, removal of cell cycle genes was done before detection of highly variable genes. Highly variable genes were detected using the Seurat pipeline to calculate the average expression and dispersion for each gene, dividing genes into bins and computing a z-score for dispersion within each group. We used a z-score of 0.5 as the dispersion cutoff and a bottom threshold of 0.0125 and high threshold of 3.0 for average expression. Linear dimensionality reduction was carried out using principal component analysis, with significant principal components (PC) selected using the elbow and jackstraw methods from Seurat. Cell clusters were identified using a shared nearest neighbor–based clustering algorithm from Seurat and subsequently visualized using t-distributed stochastic neighbor embedding.

Cell counts were normalized with the variance-stabilizing transformation method from the Seurat package (SC Transform; RRID: SCR_007322). PCs for nearest-neighbor graph construction with default "annoy Euclidian" settings were selected based on elbow plots from Principal Component Analysis and Harmony (theta 0) batch correction by the associated percent of variation. Clusters were identified with the default Seurat Louvain algorithm at 0.3 resolution. Uniform Manifold Approximation and Projection was created based on the relevant Harmony-selected PCs. Cluster markers were identified with the single-cell–adapted MAST test for differential expression and filtered for genes with more than 0.25 log fold change difference and 10% difference in percent expression and with a P value less than 0.01.

Single-cell RNA sequencing analysis

Single-cell data were normalized using the Seurat SC Transform workflow (https://satijalab.org/seurat/) and regularized with negative binomial regression (15) with mitochondrial percentage regressed out, after which, samples were integrated using Harmony (theta 0; ref. 16). PCs using nearest neighbor analysis ("annoy Euclidian") and Uniform Manifold Approximation and Projection dimension reduction were selected using a quantitative elbow plot approach by the associated percent of variation. Clusters were identified with the default Seurat Louvain algorithm at 0.3 resolution. Cluster markers and differential expression between treatments were identified using the MAST test with 0.25 log fold change threshold, 0.1% expression threshold, and minimum 10% percent expression in clusters. SC Transform normalized counts for top markers,

(*Continued.*) PDXs for both sham and 24 Gy–irradiated mice. A Student t test was performed, with P value $<2 \times 10^{-16}$. **C,** Normalized expression of the G3 recurrent signature across sham- and 24 Gy–irradiated PDXs is depicted. P values for intergroup comparisons are presented. A Student t test was performed, with P value $<2 \times 10^{-16}$. **D,** Violin plot depicting the expression of the G3 recurrent signature gene score across different medulloblastoma subgroups and normal cerebellum (CB). A Wilcoxon test was performed. P values for intergroup comparisons are presented and listed above each comparison group. **E,** Kaplan–Meier survival curves of different medulloblastoma subgroups stratified according to the expression level of the G3 recurrent signature. A high signature score is only associated with poor overall survival in G3 patients, demonstrating the specificity of this prognostic measure. A log-rank (Mantel–Cox) test was performed. **F,** Schematic of the CRISPR-mediated transcriptional activation (CRISPRa) workflow. D425-Med Cas9-VPR$^+$ cells were transduced using a custom 435 sgRNA library and engrafted followed by a low-dose irradiation schedule (3 × 2 Gy) delivered focally to the primary tumor mass to permit tumor recurrence and the emergence of radioresistant cells for next-generation sequencing. **G,** Plot depicting the enrichment of guides from the CRISPRa screen. The y-axis indicates the $\log_2$-fold change (LFC) of guides enriched in irradiated mice relative to sham controls, and the x-axis shows the FDR. Genes are labeled for the most enriched guides, and positively selected genes constituting the G3 recurrent signature are labeled in orange. BLI, bioluminescence imaging; MOI, multiplicity of infection; SHH, sonic-hedgehog; WNT, wingless.

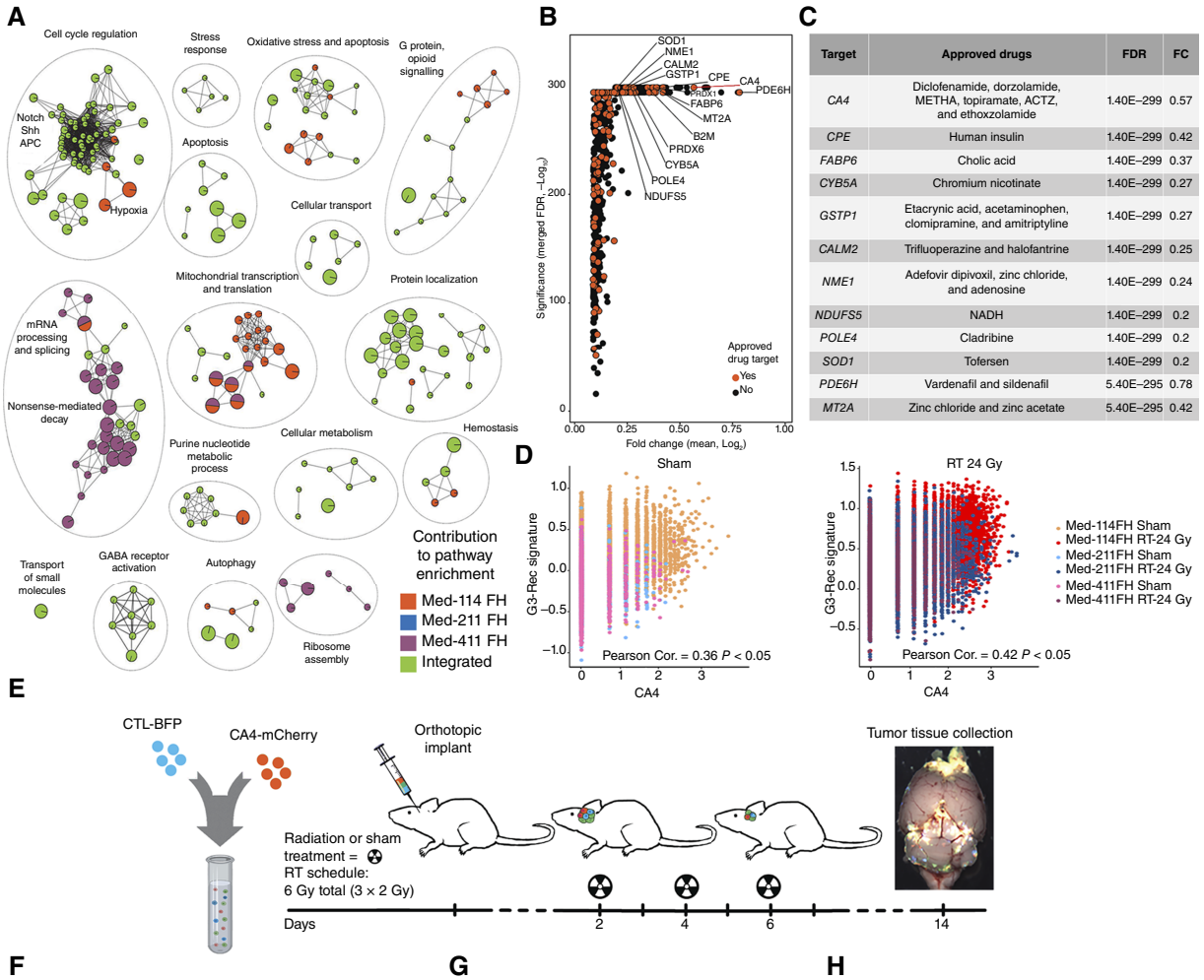

which were plotted and visualized using Seurat. Pathway analysis was performed using the gprofiler2 package (17) with multiple testing corrections and a g_SCS threshold of 0.1.

Shared differentially expressed genes between lines were sorted by mean log fold change, and for pseudo-bulk expression across single-cell clusters, the Seurat Average Expression function was used and plotted with pheatmap (https://www.rdocumentation.org/packages/pheatmap/versions/1.0.12; RRID: SCR_016418), ggplot2 (link: https://ggplot2.tidyverse.org/index.html; RRID: SCR_014601), and ggpubr (link: https://cran.r-project.org/web/packages/ggpubr/index.html) R packages. The recurrent signature was built using the AddModuleScore built-in function from the Seurat package (v.3.1.4).

CRISPR activation screen and single-guide RNA library preparation

A 435 single-guide RNA (sgRNA) library (~5 guides per gene) was generated using the top prediction hits from the CRISPR-ERA algorithm, including 50 non-targeting negative control sgRNAs (non-targeting_00000 through 00049). We synthesized sgRNA-containing oligonucleotides in a 96-well format, which were then pooled to construct sgRNA expression vectors. This was done by ligating the oligonucleotides into a common lentiviral backbone (pCRISPRia-v2, RRID: Addgene_84832) using the BstXI and BlpI restriction sites. After validating select clones using Sanger sequencing, we mixed the sgRNA constructs in equal amounts to conduct single sgRNA screens. The sgRNA sequence and corresponding genes are listed in Supplementary Table S1. Cells were transduced at a multiplicity of infection of ~0.4, puromycin selected, and intracranially engrafted into the cerebellum. MAGeCK robust rank aggregation analysis was used to identify enriched guides, and findings were plotted using MAGeCKFlute (18, 19).

In vitro cell irradiation

Cells were irradiated using the X-Rad320 X-Ray irradiator (Precision X-Ray). The following parameters were applied during irradiation: a voltage of 320 kV and a current of 12.5 mA. To administer the correct dose of irradiation, the cells were irradiated at predetermined amounts of time based on the surface area of the plate and the desired irradiation dose. Volumes and duration for 6 Gy were 100 μL and 392 seconds for 96-well plates, 500 μL and 376 seconds for 24-well plates, and 5 mL and 410 seconds for T25 flasks.

Flow cytometry

Freshly dissected samples were single cell dissociated and resuspended in PBS with 1% BSA prior to undergoing flow cytometry. Control cells were set aside and used to determine optimal voltages for side/forward scatter and fluorescence. Dead cells were excluded using either SYTOX Blue, propidium iodide, or DAPI. Flow cytometry was performed using a BD Biosciences LSRII CFI VBYR instrument, and analyses were carried out using FlowJo software (RRID: SCR_008520). In order to assess apoptosis, 100,000 cells were plated in 500 μL of media in a 24-well plate. The next day, the cells were irradiated with 1× 6 Gy with the X-Rad320 irradiator. The cells were then collected 6, 24, and 48 hours following irradiation. The cells were fixed and stained with a caspase-3 antibody (RRID: AB_393957) before analyzing via flow cytometry. This approach was repeated for phospho H2AX quantification using a γH2AX antibody (RRID: AB_1645414); however, the cells were collected 0.5, 1, and 6 hours after irradiation.

Pathway enrichment analysis

To understand the functional importance of significantly upregulated genes in RT- versus sham-treated recurrent G3 medulloblastoma PDXs, we performed an integrative pathway enrichment analysis using the ActivePathways method (20). This analysis used single-cell RNA sequencing (scRNA-seq) differential expression data from three PDXs (Med-114FH, Med-211FH, and Med-411FH), in which genes which were significantly enriched in at least one PDX were kept. The significance threshold for genes consisted of an FDR less than 0.05, an average $\log_2$-fold change greater than 0.25 (upregulated in the RT group only), and expression in at least 10% of all cells in either group (RT or sham). Genes not significant in a specific PDX were assigned a *P* value of 1 for that PDX. This resulted in 1,002 significantly upregulated human genes in at least one PDX. An integrative data matrix was formed for these 1,002 genes and included their *P* values from all three PDXs, which was then used as the input for ActivePathways. In the prioritized gene list, 513 pathways with significant overrepresentation were derived (FDR < 0.005) and visualized as an enrichment map (21). Gene sets of biological processes (gene ontology) and molecular pathways (Reactome) were analyzed via GMT files provided in the g:Profiler web server (RRID: SCR_006809; ref. 22). Gene sets were filtered by size using default parameters from the ActivePathways software.

Figure 3.

Integrative pathway enrichment analysis and druggability of significantly upregulated genes. **A,** Enrichment map of biological pathways and processes found to be upregulated in 24 Gy–treated samples using ActivePathways and visualized using Cytoscape. Nodes in the network represent similar pathways with gene interactions visualized through connecting lines. Nodes are colored by the PDX for which the pathway is enriched. Those pathways which are significantly enriched through the integration of multiple PDXs are depicted in green. **B,** Volcano plot showing the $\log_2$-fold change (*x*-axis) and FDR (*y*-axis) of significantly upregulated genes with overlapping enrichment. Fold change was calculated as the mean across all three PDXs and the FDR is derived from the adjusted *P* value after Brown *P* value integration. The druggability of genes was determined using the DrugBank and is depicted by the red nodes. **C,** Table showing the top significantly upregulated and druggable genes. Genes are ranked by FDR and mean fold change. Corresponding approved drugs for each gene are indicated. **D,** Pearson correlations of *CA4* and the G3 recurrent signature for sham- and 24 Gy–irradiated PDXs. **E,** Experimental design for orthotopic *in vivo* xenotransplantation studies using a *CA4*-overexpressing construct in G3 medulloblastoma PDX cell lines. Mice were intracranially engrafted with equal parts *BFP* control and *mCherry-CA4*–overexpressing cells and focally irradiated at the primary tumor site using a low-dose fractionated treatment schedule (3 × 2 Gy). **F,** Flow cytometry analysis of xenotransplanted Med-411FH cells expressing BFP^{+ve} control or $mCherry^{+ve}$ *CA4* overexpression constructs. **G** and **H,** Tumor cell fractions 2 weeks after engraftment are depicted showing the significant enrichment of *CA4*-overexpressing cells after RT (sham, $n = 3$; RT, $n = 6$; **G**) and insignificant change using an $mCherry^{+ve}$ control harvested 2 days after RT (**H**). A Student *t* test was performed, with *P* values listed above each comparison group. **I** and **J,** Repeating this approach for D425-Med revealed the same enrichment for *CA4*-overexpressing cells (sham, $n = 3$; RT, $n = 5$), and the use of an enzymatically defective CA4 isoform (R219S) abolished this enrichment (sham, $n = 2$; RT, $n = 3$; **K**). A Student *t* test was performed, with *P* values listed above each comparison group.

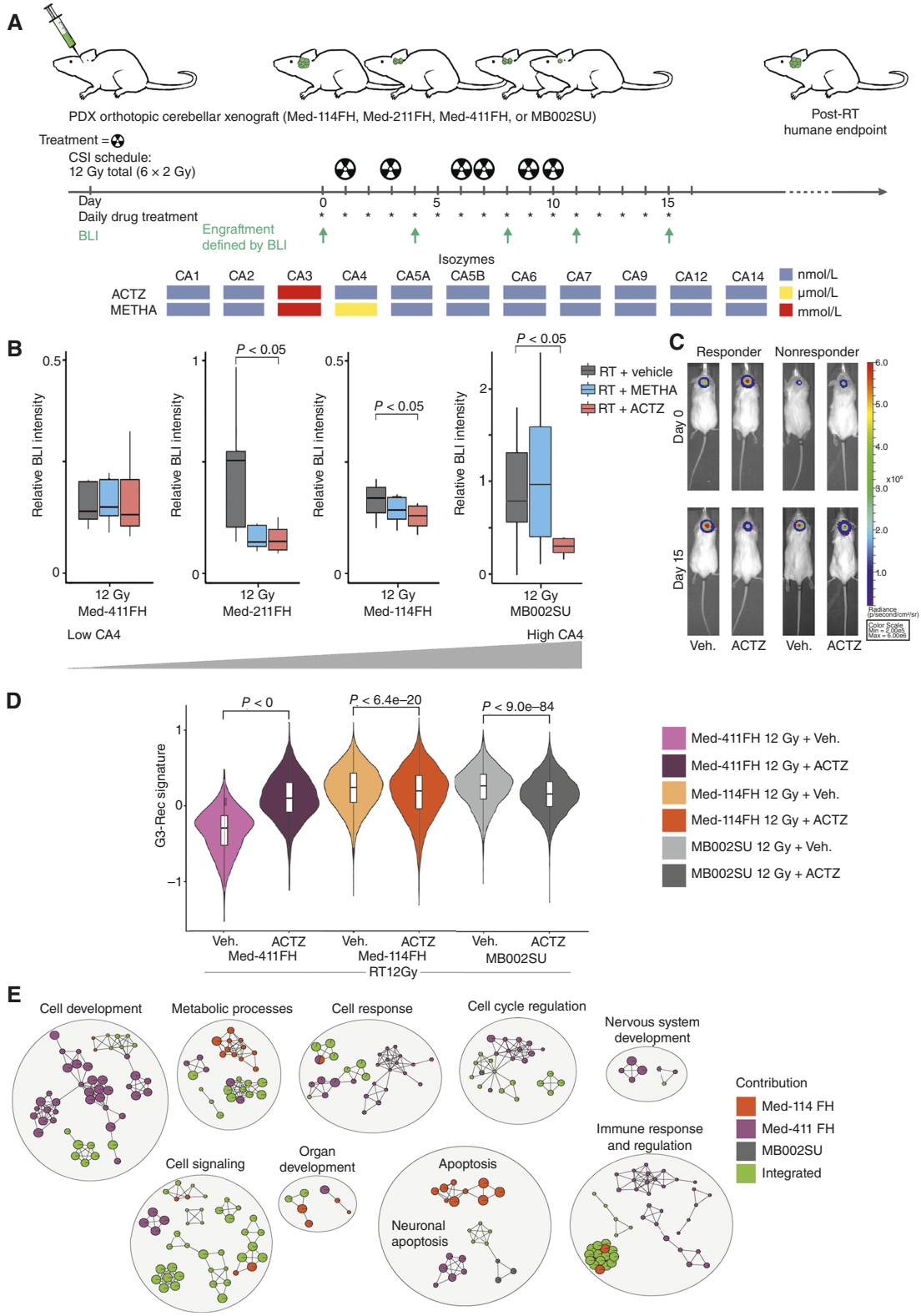

To visualize the most significantly upregulated genes in RT- versus sham-treated PDXs, we used a volcano plot to show FDR and fold change. Genes significantly upregulated in at least one PDX and overlapping an enriched pathway, which were nonsignificant in a specific PDX, were assigned a P value of 1 and $\log_2$-fold change of 0 for that PDX. A merged P value for each gene was obtained across the three PDXs using the Brown P value–merging method and then adjusted for multiple test correction (FDR). A merged $\log_2$-fold change was obtained for each gene using the mean of the average $\log_2$-fold changes across the three PDXs. The top genes by FDR (and fold change next for ties) are labeled and shown in a table. Points corresponding to genes that are druggable targets of approved drugs are shown in red based on the Human DrugBank list of approved drug targets (RRID: SCR_002700; ref. 23).

Statistical analyses

All statistical parameters (cohort size and replicates), significance, and choice of tests are reported in the associated figure legends. Survival comparisons were carried out using two-sided log-rank Mantel–Cox tests in the PDX models. For bioluminescent flux analyses, a two-sided one-way ANOVA, followed by Tukey *post hoc* test, was used. Finally, differentially expressed gene expression across publicly available microarray datasets and candidate target protein expression were analyzed using two-sided Mann–Whitney U tests. Data were deemed statistically significant when $P < 0.05$.

Survival analysis stratified by G3 radioresistant gene signature

We derived transcriptional activity scores for each transcriptional signature gene set curated by the Molecular Signature Database ($n = 21{,}450$) in a cohort of patients with medulloblastoma with a clinically annotated transcriptional dataset (24, 25). Then we stratified the cohort into high versus low groups using the median transcriptional signature score as the cutoff and performed the log-rank test in Kaplan–Meier survival analysis with FDR adjustment (26).

Data availability

The data generated in this study are publicly available through EMBL-EBI's ArrayExpress at E-MTAB-15292. All other raw data generated in this study are available upon request from the corresponding authors.

Results

Modeling radiation resistance in G3 medulloblastoma

As radiation is the single most effective current therapy for medulloblastoma, we sought to understand RT resistance in G3 medulloblastoma. Although most children with G3 medulloblastoma undergo both RT and cytotoxic chemotherapy, murine models can tolerate either CSI or high-dose chemotherapy but not both; we chose to focus on RT. In a mouse hospital approach, we provided CT-guided RT to three established PDX models of G3 medulloblastoma (Med-411FH, Med-211FH, and Med-114FH; **Fig. 1A**; ref. 10). All three of these PDX models belong to the aggressive G3γ subtype of medulloblastoma (Supplementary Fig. S1A and S1B). These therapy-naïve PDX lines were injected into the cerebellum of immunodeficient mice, and engraftment was documented using bioluminescence. Engrafted mice were treated with RT regimens similar to human protocols using 24 Gy or 36 Gy (**Fig. 1A**; Supplementary Fig. S1C). Mice were randomized to either sham irradiation, standard-dose irradiation (24 Gy), or high-dose irradiation (36 Gy), with all doses of radiation providing better survival than sham-irradiated controls (**Fig. 1B–E**). Animals treated with 36 Gy did not relapse in the central nervous system but rather with extensive disease in the liver, lungs, and lymph nodes (Supplementary Fig. S1D–S1F). This is very distinct from the pattern of recurrence of G3 medulloblastoma in human children, in whom relapse is almost exclusively in the leptomeninges, with extraneural metastases being very uncommon. Conversely, animals treated with 24 Gy irradiation relapsed in the leptomeninges, a pattern nearly identical to human patients. We noted that although sham-irradiated animals tended to expire from tumor at the primary injection site, irradiated animals recurred distally in the leptomeninges (Supplementary Fig. S1G and S1H).

Radiation response in G3 medulloblastoma models

Single-cell transcriptomics offers a unique opportunity to understand the cell-autonomous cellular biology of model systems and is particularly useful in the study of clonal neoplasms. scRNA-seq of sham- versus 24 Gy–irradiated therapy-naïve G3 PDXs revealed cell-autonomous transcriptional differences between sham and irradiated tumors (**Fig. 1F**; Supplementary Fig. S2A–S2F). Tumor cells treated with 24 Gy as compared with sham-irradiated tumors demonstrated a decreased expression of stem cell programs and an increased proliferative signature across all three irradiated PDX lines (**Fig. 1G**; Supplementary Fig. S2G and S2H). Five genes that underwent increased transcription in all three experimental irradiated lines [peroxiredoxin 1 (*PRDX1*), peroxiredoxin 4 (*PRDX4*), ubiquitin C-terminal hydrolase L1 (*UCHL1*), neuronal pentraxin 1 (*NPTX1*), and ubiquitin-conjugating enzyme E2 S (*UBE2S*)] were used to define a G3 medulloblastoma gene expression signature (26) for high risk of post-irradiation recurrence (**Fig. 2A–C**). The prognostic importance of this five-gene signature was specific to G3 medulloblastoma as compared with wingless, sonic-hedgehog, or G4 medulloblastoma across a cohort of human patients (**Fig. 2D** and **E**; Supplementary Fig. 3A; ref. 27). Although the five-gene signature

Figure 4.

Radiosensitization of G3 medulloblastoma through the inhibition of CA4. **A,** Design of *in vivo* orthotopic xenotransplantation studies and treatment schedule for CA inhibitors. Mice were administered using fractionated (6 × 2Gy) CSI and daily drug treatments (two doses of 50 mg/kg) of a select inhibitor or a polyethylene glycol control. The specificity of ACTZ and METHA is depicted by the concentration of drug required to achieve the targeted inhibition of each CA isozyme. **B,** Quantification of the average bioluminescence (BLI) signal from each treatment group. Relative luminescence as quantified through normalization to pre-irradiated (day 0) mice for Med-114FH, Med-211FH, Med-411FH, and MB002SU PDX cell lines. A two-sided one-way ANOVA followed by the Tukey *post hoc* test was used, with P values listed where significant. **C,** Representative image of the bioluminescence signal observed at the start of treatment (day 0) and after the last treatment (day 15) in a responder and nonresponder PDX cell line. **D,** Violin plot quantifying the G3 recurrent signature across treatment-naïve PDX lines after RT with vehicle (Veh.) or ACTZ treatment. A Wilcoxon test was performed, with P values listed above each comparison group. **E,** Biological pathways found to be enhanced in both CA4-high PDX cell lines (MB002SU and Med-114FH) after RT with ACTZ- vs. vehicle-treated samples. Nodes are colored by the PDX in which the pathway is enriched or labeled as integrated for pathways detected from the merged signal of both PDXs but neither alone.

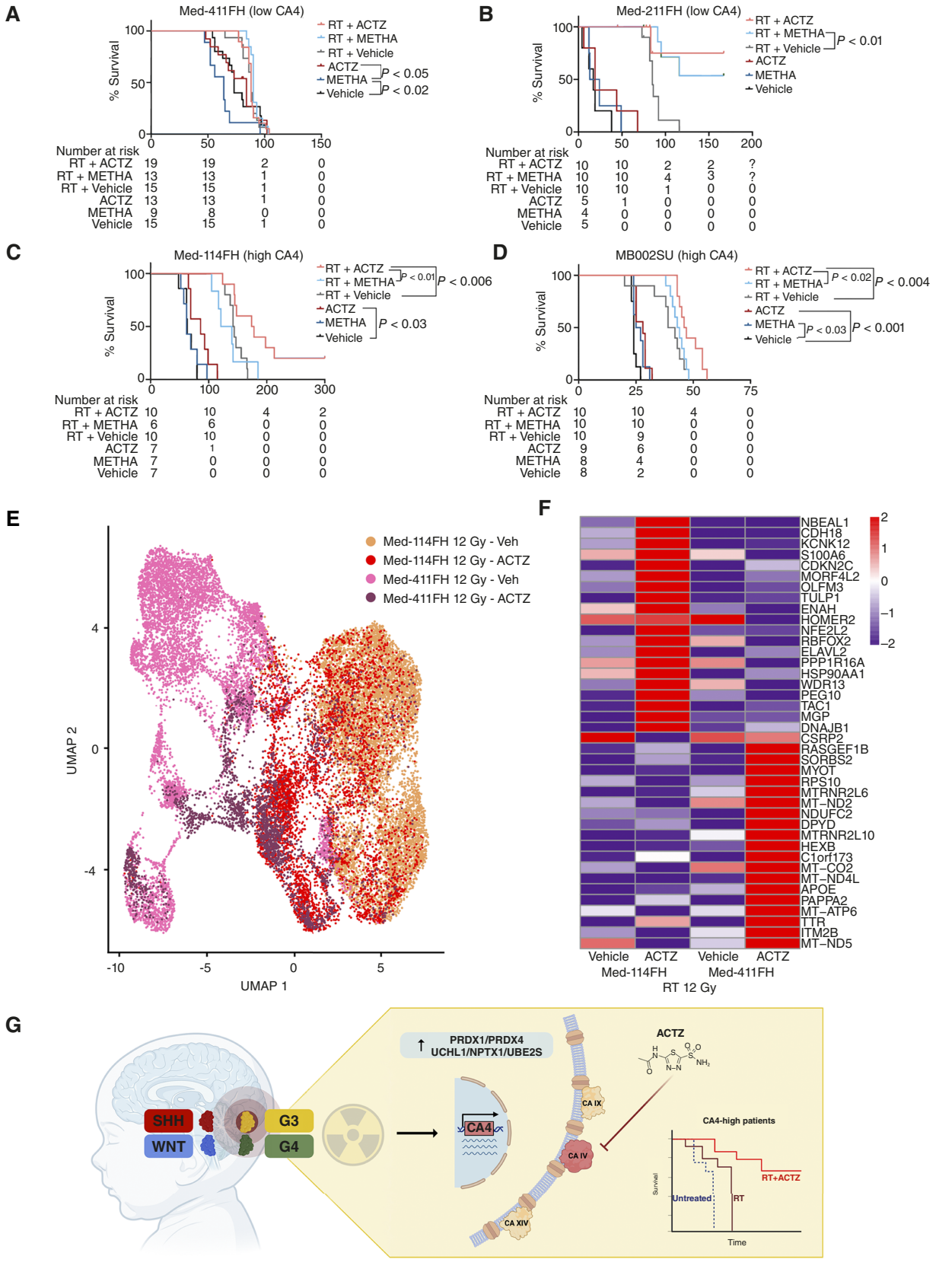

was highly prognostic, no single gene alone was predictive (Supplementary Fig. S3B). This five-gene signature also correlated with increased metastatic burden at presentation (Supplementary Fig. S3C and S3D), another known risk factor for medulloblastoma recurrence. To discern whether the five genes in our risk signature were correlative versus causative, we undertook a gain-of-function CRISPR screen (28) using an additional G3 medulloblastoma cell line (D425-Med), with a library of guides targeting all genes that were found to be upregulated after irradiation in at least two of the PDXs illustrated in **Fig. 1F**. CRISPR-transduced D425-Med cells were engrafted into immunodeficient mice prior to RT (6 Gy) or sham irradiation (**Fig. 2F**). The dose of radiation was reduced in this experiment to deliberately foster the development of radiation resistance. Tumors at endpoint were deeply sequenced to determine the relative representation of bar-coded CRISPR guides (18, 19). Notably, three of the five genes in our high-risk five-gene signature were enriched in the irradiated tumors as compared with sham-irradiated controls, suggesting that they help to drive radioresistance *in vivo* (**Fig. 2G**). These data are consistent with a model in which transcriptional changes after RT are indicative of the underlying biology of radioresistance in G3 medulloblastoma.

Druggable genes driving radioresistance in G3 medulloblastoma

As the transcriptional changes after RT in G3 medulloblastoma seemed to identify biology causatively underlying radioresistance, we used the single-cell dataset presented in **Fig. 1** to identify overrepresented genes and pathways in each of the three PDX lines (**Fig. 3A**, FDR < 0.005; ref. 20). Given that none of the five genes in our G3 radioresistance gene signature is targeted by a currently approved drug, we sought to identify commonalities that might be therapeutically leveraged. The DrugBank database was used to nominate putative targets from the list of genes with increased expression after RT for which there are FDA-approved drugs (**Fig. 3B** and **C**). The top candidate gene to emerge from this analysis was the metalloenzyme CA4 (**Fig. 3C**). The CA4 protein catalyzes the conversion of carbon dioxide to bicarbonate, and other cancers expressing high levels of CA-IX or CA-XII are reported to be less responsive to radiation whereby their inhibition significantly increases radiosensitivity (27–32). There are several isozymes of CA in humans; however, only CA4 is highly expressed in G3 medulloblastoma (Supplementary Fig. S4A and S4B). We demonstrated that the expression level of CA4 in G3 medulloblastoma increased after 24 Gy of irradiation in two of the three experimental PDX lines studied (Supplementary Fig. S5A–S5C). Pearson correlations were carried out for sham- and 24 Gy–irradiated samples showing a significant correlation between *CA4* expression and our five-gene recurrence signature subsequent to irradiation. Both signatures were notably elevated even among lines with low levels of endogenous *CA4* expression (**Fig. 3D**; Supplementary Fig. S5D and S5E). These data support a model in which both endogenous and radiation-driven levels of CA4 protein protect G3 medulloblastoma cells from radiation and FDA-approved anti-CA4 drugs could improve the response to RT.

CA4 promotes G3 medulloblastoma radioresistance *in vivo*

The PDX cell line Med-411FH was identified as having a low endogenous level of CA4 (Supplementary Figs. S4B and S5A). Leveraging this finding, Med-411FH was engineered to overexpress a fluorescently tagged *CA4* cDNA. Immunodeficient mice were simultaneously xenografted with equal numbers of Med-411FH cells expressing either *CA4* (*mCherry*) or an empty vector control blue fluorescent protein (*BFP*) to conduct *in vivo* competition assays. Bioluminescent evidence for tumor engraftment from the mixture of reporter cells was followed by fractionated RT to a total dose of 6 Gy (**Fig. 3E**). Two weeks after irradiation, the animals were sacrificed and the tumors were removed to quantify the relative proportion of $mCherry^{+ve}$ versus BFP^{+ve} cells (**Fig. 3F–H**; Supplementary Fig. S5F–S5H). The relative enrichment for $mCherry^{+ve}$ cells in the post-irradiation setting was consistent with an active role of the CA4 protein in the promotion of radiation resistance. Repeating this *in vivo* cell competition assay after irradiation in a second G3 medulloblastoma cell line (D425-Med) also demonstrated a clonal advantage after RT for cells expressing high levels of CA4 (**Fig. 3I** and **J**).

To discern whether the *in vivo* phenotype observed is specific to the catalytic activity of CA4, we repeated our *in vivo* competition assay using a $CA4^{R219S}$ point mutant (*CA4-Mut*) that lacks catalytic activity mirroring the inhibitory effect of sulfonamides. As *CA4-Mut* did not drive a clonal advantage *in vivo* after irradiation, we concluded that the radioresistant effects of CA4 are largely due to its catalytic activity (**Fig. 3K**; ref. 29).

To assess the effect of *CA4* expression on cell survival, D425-Med cells were transduced with a *CA4* construct resulting in a significant reduction in caspase-3 activation 24 hours after irradiation when compared with both wild-type and catalytically inactive *CA4-Mut* cells (Supplementary Fig. S6A and S6B). In contrast, increased caspase activation was observed through the short hairpin RNA inhibition of *CA4* in MB002SU cells.

To address DNA double-strand break (DSB) repair pathways, we examined phospho-histone H2AX (γH2AX) in D425-Med and MB002SU cells following irradiation. Time course experiments in D425-Med cells overexpressing *CA4* showed significantly reduced

Figure 5.

Inhibition of CA4 diminishes RT resistance. **A,** Kaplan–Meier survival curves of G3 engrafted mice using different therapeutic regimens. Overall survival is presented for Med-411FH treated with vehicle + RT ($n = 15$), ACTZ + RT ($n = 19$), METHA + RT ($n = 13$), vehicle ($n = 15$), ACTZ ($n = 13$), and METHA ($n = 9$) without RT. **B,** Overall survival for Med-211FH treated with vehicle + RT ($n = 10$), ACTZ + RT ($n = 10$), METHA + RT ($n = 10$), vehicle ($n = 5$), ACTZ ($n = 5$), and METHA ($n = 4$) without RT. **C,** Overall survival for Med-114FH treated with vehicle + RT ($n = 10$), ACTZ + RT ($n = 10$), METHA + RT ($n = 6$), vehicle ($n = 7$), ACTZ ($n = 7$), and METHA ($n = 7$) without RT. **D,** MB002SU treated with vehicle + RT ($n = 10$), ACTZ + RT ($n = 10$), METHA + RT ($n = 10$), vehicle ($n = 8$), ACTZ ($n = 8$), and METHA ($n = 8$) without RT. A log-rank (Mantel–Cox) test was performed, with *P* values listed where significant. **E,** Uniform Manifold Approximation and Projection (UMAP) of single-cell expression data from irradiated (12 Gy) mice treated with ACTZ or vehicle contrasting CA4-high and -low PDXs (Med-114FH and Med-411FH, respectively). Comparison of the treated clusters reveals a distinct transcriptional change after ACTZ treatment with variable clustering between CA4-high– and CA4-low–expressing tumors. **F,** Heatmap reporting the expression of discriminative gene sets between CA4-high (Med-114FH) and -low (Med-411FH) PDXs filtered using vehicle controls. Distinct transcriptional regulatory programs are apparent after ACTZ treatment, with similar baseline expression noted in the vehicle controls. **G,** Schematic summarizing the transcriptional changes that occur in G3 medulloblastoma after RT and the inhibition of CA4 as a novel therapeutic strategy. After irradiation, G3 medulloblastoma expresses a subgroup-specific gene signature accompanied by an increase in CA4 promoting radioresistance. Treatment using the FDA-approved drug ACTZ decreases tumor burden and increases survival for CA4-high–expressing tumors, presenting CA4 as a novel predictive biomarker. SHH, sonic-hedgehog; WNT, wingless.

DNA damage reflected by a reduction in γH2AX staining, whereas the overexpression of *CA4-Mut* also reduced DNA damage, suggesting enzyme-independent mechanisms of mediating DSB repair kinetics (Supplementary Fig. S6D and S6E). The silencing of *CA4* in MB002SU via short hairpin RNA did not show any appreciable change in DNA damage relative to control cells after irradiation (Supplementary Fig. S6F and S6G). This may indicate that the downregulation of *CA4* is insufficient to affect DSB repair, suggesting that CA4 promotes survival through alternative means or alongside redundant mechanisms.

These data are consistent with a model in which CA4 is sufficient to drive radioresistance in G3 models of medulloblastoma and that its enzymatic activity *in vivo* is critical to this process and therefore possibly druggable in both model systems and human patients.

Drugs targeting CA4 diminish RT resistance of G3 medulloblastoma

We hypothesized that FDA-approved drugs that inhibit the enzymatic activity of CAs could diminish RT resistance and increase survival in our G3 medulloblastoma model systems. Mice were xenografted with four patient-derived G3 cell lines (Med-114FH, Med-211FH, Med-411FH, and MB002SU) and allowed to grow until baseline bioluminescence. These PDX lines demonstrate variable levels of endogenous CA4 expression (Supplementary Fig. S5A). Engrafted mice were treated with fractionated CSI ± the pan CA inhibitor ACTZ or the inhibitor METHA, which carries comparable activity but with poor efficacy for CA4, or a polyethylene glycol (vehicle) control (**Fig. 4A**; refs. 30, 31). To sensitize our mouse models, we administered a subtherapeutic dose of RT (12 Gy total) to determine whether CA inhibitors could contribute to tumor inhibition. We observed diminished tumor bioluminescence in three of four PDX model systems when treated with ACTZ as compared with METHA (**Fig. 4B** and **C**), with the nonresponder (Med-411FH) not exhibiting an increase in CA4 expression after RT. Med-211FH was observed to exhibit elevated expression of *CA7* (Supplementary Fig. S4B); thus, to have a narrowed picture of transcriptional changes related to CA4 inhibition, it was omitted from scRNA-seq analysis. The single-cell transcriptomics of tumors treated with both RT and ACTZ as compared with controls demonstrated diminished expression of our G3 medulloblastoma five-gene recurrence signature (**Fig. 4D**), other than the Med-411FH nonresponder. Comparison of the transcriptomes of tumor cells from the treatment-naïve PDXs with the highest expression of *CA4* versus the lowest demonstrated increased expression of genes in pathways related to the mitochondrial respiratory chain, response to radiation, and apoptosis (**Fig. 4E**).

The administration of ACTZ after irradiation conferred no significant increase in survival relative to controls for either of the endogenously low CA4-expressing PDXs (**Fig. 5A** and **B**). Med-411FH demonstrated no therapeutic benefit of ACTZ therapy during RT, consistent with unchanged bioluminescence and an increase in recurrent signature after treatment. We also did not observe a survival benefit for Med-211FH despite mildly elevated CA4 expression after irradiation. By contrast, both PDXs expressing high levels of CA4 (Med-114FH and MB002SU) showed significantly reduced bioluminescence, decreased expression of our five-gene recurrence signature, and a significant increase in overall survival when RT was supplemented with ACTZ (**Fig. 5C** and **D**). We compared the transcriptional profiles of a responder and nonresponder after ACTZ radiosensitization (Med-114FH and Med-411FH; **Fig. 5E**; Supplementary Fig. S7), demonstrating unique transcriptional changes after RT between these PDXs (**Fig. 5F**). These transcriptional differences and associated signaling pathways are reported in Supplementary Tables S2 and S3. Moreover, we found a decreased cell cycle signature indicative of reduced proliferation in the responder PDX (Supplementary Fig. S7C). These findings support the therapeutic benefit of administering ACTZ as an adjuvant to RT in CA4-high expressing tumors (**Fig. 5G**).

Discussion

G3 medulloblastoma is associated with a high mortality, and there is an unmet need for new therapeutic strategies that improve the efficacy of treatment and reduce the risk of tumor recurrence. Here, we used PDX models to define G3 medulloblastoma responses to treatment with CSI. Our data revealed a prognostic signature and a clinically actionable biomarker that underlies G3 medulloblastoma radioresistance and recurrence after therapy that may improve clinical outcomes for children with the most common malignant brain tumor.

Our scRNA-seq data revealed gene expression programs driving G3 medulloblastoma resistance to RT across three distinct human patient-derived models. Using these data, we established a prognostic gene expression risk score based on the most expressed genes in post-RT samples from the time of recurrence. We found that this G3-specific signature could serve as an independent measure of poor prognosis in G3 medulloblastomas, suggesting that these genes might play a role in resistance to RT. These findings underscore the translational role for this risk signature to stratify upfront high-risk groups that have differentially enriched pathways with distinct oncogenic properties, which may be leveraged to better direct the course of treatment. Among the genes in this risk stratification signature, we found peroxiredoxins 1 and 4 (*PRDX1* and *PRDX4*), *UCHL1*, *NPTX1*, and *UBE2S* to be enriched after RT. Peroxiredoxins are a family of thiol peroxidases that maintain the intracellular redox balance and protect organisms against oxidative stress (32), and the function of *PRDX* genes in medulloblastoma pathogenesis or response to treatment was previously unknown. Mammalian cells possess six PRDX isoforms, which are antioxidant enzymes that regulate multiple cellular programs, including reactive oxygen species–dependent signaling pathways that play a role in the progression and metastasis of other cancer types (33–36). The ubiquitin C-terminal hydrolase (UCH) family of deubiquitinating enzymes is comprised of four members, of which, *UCHL1* is highly expressed in brain tissue and is indispensable for neuronal development and axonal maintenance and integrity (37–39). Mutations in the *UCHL1* gene in humans are associated with progressive early-onset neurodegeneration, and *UCHL1* expression can be dysregulated in various tumor types and is associated with TGFβ signaling–induced cancer invasion and metastasis by protecting the TGFβ type I receptor and SMAD2 from ubiquitination (40). *NPTX1* is a member of the pentraxin gene family that is exclusively expressed in the nervous system (41). Pentraxins (PTX) are an evolutionarily conserved family of proteins that have a unique protein domain that mediates synaptic function as well as metastasis in pancreatic cancer (42) through the uptake of synaptic macromolecules and remodeling of synaptic plasticity (43, 44). Finally, UBE2S, which mediates target ubiquitination (42, 45–47), acts as an essential factor in the anaphase-promoting complex/cyclosome, a cell cycle–regulated ubiquitin ligase that controls progression through mitosis. *UBE2S* expression strongly correlates with poor prognosis and resistance to chemoradiotherapy in gliomas (48–51). Elucidating the function of these genes, their regulation, and whether they are also

important in other molecular subgroups of medulloblastoma or different cancer types requires further investigation.

In our preclinical studies reported here, we found that the expression of CA4 increased after RT. CA4 is a member of the carbonic anhydrase (CA) family and its expression was found to be restricted to the G3 and G4 molecular subgroups of medulloblastoma. CA4 is a membrane-associated glycosylphosphatidylinositol-linked protein and essential component of the pH-regulatory system through the production of bicarbonate at the extracellular surface, which helps to maintain an alkaline pH when transported intracellularly and consequently contributes to the acidification of the extracellular space (52). Exposure to RT induces oxidative damage and these radio-induced radicals are mostly dependent on pH (53).

The clinical importance of these observations may be significant as therapy for medulloblastoma has remained largely unchanged for the last 20 years, and concerns about therapy-related late toxicities have prompted systematic attempts at treatment deintensification. These trials (in low-risk medulloblastoma) that omitted upfront CSI ended early because of high relapse rates, suggesting that despite potential toxicities, CSI remains an integral component of treatment. Here, we tested the hypothesis that tumor cells expressing CA4 might be positively selected as a part of the adaptative response to RT. We present evidence that the overexpression of CA4 is capable of conferring radioresistance and that impairing its enzymatic activity radiosensitizes tumors to treatment. Thus, targeted therapeutics against CA4 may be useful as adjuvant therapies alongside conventional ionizing radiation and may increase the efficacy of treatment in patients. ACTZ in responders leads to the regulation of different sets of genes and pathways compared with nonresponders (Supplementary Fig. S7G; Supplementary Tables S2 and S3). Further studies, including detailed molecular profiling and *in vivo* analyses, will be crucial to fully understand the factors driving these different clinical outcomes.

Several FDA-approved CA4 inhibitors exist and can cross the blood–brain barrier (54), suggesting the importance of re-evaluating these agents in the context of pediatric brain tumors for clinical translation. As the mortality rate for G3 medulloblastoma is very high (3) and given that the FDA-approved drug ACTZ has been routinely used in neurosurgery patients to treat elevated intracranial pressure, we propose that a clinical trial of radiosensitization using ACTZ could be considered in this subgroup of patients, for which there are currently no available rational therapies.

Authors' Disclosures

A. Guerreiro Stücklin reports other support from Alexion and Novartis outside the submitted work. C. Daniels reports grants from Hospital for Sick Children and Baylor College of Medicine during the conduct of the study. M.D. Taylor reports grants from Hospital for Sick Children and Baylor College of Medicine during the conduct of the study. No disclosures were reported by the other authors.

Authors' Contributions

C.M. Richman: Conceptualization, investigation, writing–original draft. **A. Rasnitsyn:** Data curation, software, investigation. **B.L. Holgado:** Data curation, software, validation, investigation. **M. Vladoiu:** Validation, investigation. **N. Abeysundara:** Validation, investigation. **S. Majo:** Formal analysis, validation, investigation. **S. Chabi:** Formal analysis, validation. **L.J. Taunay:** Validation, investigation. **H. Suzuki:** Data curation, formal analysis, investigation, methodology. **I. Shibahara:** Data curation, formal analysis, methodology. **J. Haapasalo:** Formal analysis, investigation, methodology. **J.G. Pallotta:** Investigation, methodology. **T. Douglas:** Investigation, methodology. **K. Kharas:** Investigation, methodology. **K. Juraschka:** Formal analysis, validation, investigation. **O. Ocsenas:** Data curation, methodology. **S.A. Kumar:** Validation, investigation, methodology. **K. Nordfors:** Supervision, validation, investigation, methodology. **A. Guerreiro Stücklin:** Supervision, validation, investigation, methodology. **R.A. Suarez:** Validation, investigation. **J. Zhang:** Data curation, validation, investigation, methodology. **X. Wu:** Supervision, investigation, methodology, project administration. **C. Daniels:** Supervision, investigation, project administration, writing–review and editing. **L. Garzia:** Resources, supervision, funding acquisition, project administration, writing–review and editing. **J. Reimand:** Conceptualization, resources, supervision, investigation, writing–review and editing. **O. Saulnier:** Conceptualization, resources, validation, investigation, writing–original draft, writing–review and editing. **T.E. Merchant:** Conceptualization, validation, investigation, visualization, writing–review and editing. **C. Pouponnot:** Conceptualization, validation, visualization, writing–review and editing. **D.R. Raleigh:** Conceptualization, resources, supervision, visualization, writing–review and editing. **M.D. Taylor:** Conceptualization, resources, supervision, funding acquisition, validation, investigation, visualization, writing–original draft, writing–review and editing. **P. De Antonellis:** Conceptualization, resources, supervision, funding acquisition, validation, investigation, writing–original draft, writing–review and editing.

Acknowledgments

M.D. Taylor is a Cancer Prevention and Research Institute of Texas Scholar in Cancer Research (CPRIT - RR220051). M.D. Taylor is the Cyvia and Melvyn Wolff Chair of Pediatric Neuro-Oncology, Texas Children's Cancer and Hematology Center. M.D. Taylor is supported by the NIH (R01NS106155, R01CA159859, and R01CA255369), The Pediatric Brain Tumour Foundation, The Terry Fox Research Institute, The Canadian Institutes of Health Research, The Cure Search Foundation, Matthew Larson Foundation (IronMatt), b.r.a.i.n.child, Meagan's Walk, SWIFTY Foundation, The Brain Tumour Charity, Genome Canada, Genome BC, Genome Quebec, the Ontario Research Fund, Worldwide Cancer Research, V-Foundation for Cancer Research, and the Ontario Institute for Cancer Research through funding provided by the Government of Ontario. M.D. Taylor is also supported by a Canadian Cancer Society Research Institute Impact grant, a Cancer Research UK Brain Tumour Award, and by a Stand Up To Cancer (SU2C) - St. Baldrick's Pediatric Dream Team Translational Cancer Research Grant, Grant Number SU2C-AACR-DT11-13, and SU2C Canada Cancer Stem Cell Dream Team Research Grant (SU2C-AACR-DT-19-15) provided by the Government of Canada through Genome Canada and the Canadian Institutes of Health Research, with supplemental support from the Ontario Institute for Cancer Research, through funding provided by the Government of Ontario. SU2C Canada is a Canadian Registered Charity (Reg. #80550 6730 RR0001). Research Funding is administered by the American Association for Cancer Research International – Canada, the Scientific Partner of SU2C Canada. P. De Antonellis was supported by the Italian Association for Cancer Research (#17881). The authors would like to thank P. Zoppoli (Federico II University of Naples, Department of Molecular Medicine and Medical Biotechnology) for his advice and bioinformatic guidance. The authors would also like to acknowledge "The Centre for Phenogenomics" veterinary staff and animal technicians for colony management and monitoring and the Spatio-Temporal Targeting and Amplification of Radiation Response program and its affiliated funding agencies.

Note

Supplementary data for this article are available at Cancer Research Online (http://cancerres.aacrjournals.org/).

Received October 21, 2024; revised April 18, 2025; accepted July 17, 2025; posted first July 25, 2025.

References

1. Sharma T, Schwalbe EC, Williamson D, Sill M, Hovestadt V, Mynarek M, et al. Second-generation molecular subgrouping of medulloblastoma: an international meta-analysis of Group 3 and Group 4 subtypes. Acta Neuropathol 2019;138:309–26.
2. Okonechnikov K, Federico A, Schrimpf D, Sievers P, Sahm F, Koster J, et al. Comparison of transcriptome profiles between medulloblastoma primary and recurrent tumors uncovers novel variance effects in relapses. Acta Neuropathol Commun 2023;11:7.

3. Amayiri N, Swaidan M, Ibrahimi A, Hirmas N, Musharbash A, Bouffet E, et al. Molecular subgroup is the strongest predictor of medulloblastoma outcome in a Resource-Limited country. JCO Glob Oncol 2021;7:1442–53.
4. Northcott PA, Shih DJ, Peacock J, Garzia L, Morrissy AS, Zichner T, et al. Subgroup-specific structural variation across 1,000 medulloblastoma genomes. Nature 2012;488:49–56.
5. Northcott PA, Jones DT, Kool M, Robinson GW, Gilbertson RJ, Cho YJ, et al. Medulloblastomics: the end of the beginning. Nat Rev Cancer 2012;12:818–34.
6. Erker C, Mynarek M, Bailey S, Mazewski CM, Baroni L, Massimino M, et al. Outcomes of infants and young children with relapsed medulloblastoma after initial craniospinal irradiation-sparing approaches: an international cohort study. J Clin Oncol 2023;41:1921–32.
7. O'Halloran K, Phadnis S, Friedman GK, Metrock K, Davidson TB, Robison NJ, et al. Effective re-induction regimen for children with recurrent medulloblastoma. Neurooncol Adv 2024;6:vdae070.
8. Hill RM, Richardson S, Schwalbe EC, Hicks D, Lindsey JC, Crosier S, et al. Time, pattern, and outcome of medulloblastoma relapse and their association with tumour biology at diagnosis and therapy: a multicentre cohort study. Lancet Child Adolesc Health 2020;4:865–74.
9. Hill RM, Plasschaert SLA, Timmermann B, Dufour C, Aquilina K, Avula S, et al. Relapsed medulloblastoma in pre-irradiated patients: current practice for diagnostics and treatment. Cancers (Basel) 2021;14:126.
10. Brabetz S, Leary SES, Gröbner SN, Nakamoto MW, Şeker-Cin H, Girard EJ, et al. A biobank of patient-derived pediatric brain tumor models. Nat Med 2018;24:1752–61.
11. Bandopadhayay P, Bergthold G, Nguyen B, Schubert S, Gholamin S, Tang Y, et al. BET bromodomain inhibition of MYC-amplified medulloblastoma. Clin Cancer Res 2014;20:912–25.
12. Donovan LK, Delaidelli A, Joseph SK, Bielamowicz K, Fousek K, Holgado BL, et al. Locoregional delivery of CAR T cells to the cerebrospinal fluid for treatment of metastatic medulloblastoma and ependymoma. Nat Med 2020;26:720–31.
13. Morrissy AS, Garzia L, Shih DJ, Zuyderduyn S, Huang X, Skowron P, et al. Divergent clonal selection dominates medulloblastoma at recurrence. Nature 2016;529:351–7.
14. Vladoiu MC, El-Hamamy I, Donovan LK, Farooq H, Holgado BL, Sundaravadanam Y, et al. Childhood cerebellar tumours mirror conserved fetal transcriptional programs. Nature 2019;572:67–73.
15. Hafemeister C, Satija R. Normalization and variance stabilization of single-cell RNA-seq data using regularized negative binomial regression. Genome Biol 2019;20:296.
16. Korsunsky I, Millard N, Fan J, Slowikowski K, Zhang F, Wei K, et al. Fast, sensitive and accurate integration of single-cell data with harmony. Nat Methods 2019;16:1289–96.
17. Kolberg L, Raudvere U, Kuzmin I, Vilo J, Peterson H. gprofiler2—an R package for gene list functional enrichment analysis and namespace conversion toolset g:Profiler. F1000Res 2020;9:ELIXIR-709.
18. Li W, Xu H, Xiao T, Cong L, Love MI, Zhang F, et al. MAGeCK enables robust identification of essential genes from genome-scale CRISPR/Cas9 knockout screens. Genome Biol 2014;15:554.
19. Wang B, Wang M, Zhang W, Xiao T, Chen CH, Wu A, et al. Integrative analysis of pooled CRISPR genetic screens using MAGeCKFlute. Nat Protoc 2019;14:756–80.
20. Paczkowska M, Barenboim J, Sintupisut N, Fox NS, Zhu H, Abd-Rabbo D, et al. Integrative pathway enrichment analysis of multivariate omics data. Nat Commun 2020;11:735.
21. Reimand J, Isserlin R, Voisin V, Kucera M, Tannus-Lopes C, Rostamianfar A, et al. Pathway enrichment analysis and visualization of omics data using g:Profiler, GSEA, Cytoscape and EnrichmentMap. Nat Protoc 2019;14:482–517.
22. Reimand J, Kull M, Peterson H, Hansen J, Vilo J. g:Profiler—a web-based toolset for functional profiling of gene lists from large-scale experiments. Nucleic Acids Res 2007;35:W193–200.
23. Wishart DS, Feunang YD, Guo AC, Lo EJ, Marcu A, Grant JR, et al. DrugBank 5.0: a major update to the DrugBank database for 2018. Nucleic Acids Res 2018;46:D1074–82.
24. Liberzon A, Birger C, Thorvaldsdóttir H, Ghandi M, Mesirov JP, Tamayo P. The molecular signatures database (MSigDB) hallmark gene set collection. Cell Syst 2015;1:417–25.
25. Witt H, Mack SC, Ryzhova M, Bender S, Sill M, Isserlin R, et al. Delineation of two clinically and molecularly distinct subgroups of posterior fossa ependymoma. Cancer Cell 2011;20:143–57.
26. Hovestadt V, Smith KS, Bihannic L, Filbin MG, Shaw ML, Baumgartner A, et al. Resolving medulloblastoma cellular architecture by single-cell genomics. Nature 2019;572:74–9.
27. Cavalli FMG, Remke M, Rampasek L, Peacock J, Shih DJH, Luu B, et al. Intertumoral heterogeneity within medulloblastoma subgroups. Cancer Cell 2017;31:737–54.e6.
28. Gilbert LA, Horlbeck MA, Adamson B, Villalta JE, Chen Y, Whitehead EH, et al. Genome-scale CRISPR-mediated control of gene repression and activation. Cell 2014;159:647–61.
29. Yang Z, Alvarez BV, Chakarova C, Jiang L, Karan G, Frederick JM, et al. Mutant carbonic anhydrase 4 impairs pH regulation and causes retinal photoreceptor degeneration. Hum Mol Genet 2005;14:255–65.
30. Supuran CT. Carbonic anhydrases: novel therapeutic applications for inhibitors and activators. Nat Rev Drug Discov 2008;7:168–81.
31. Neri D, Supuran CT. Interfering with pH regulation in tumours as a therapeutic strategy. Nat Rev Drug Discov 2011;10:767–77.
32. Rhee SG, Woo HA, Kil IS, Bae SH. Peroxiredoxin functions as a peroxidase and a regulator and sensor of local peroxides. J Biol Chem 2012;287:4403–10.
33. Kim TH, Song J, Kim SH, Parikh AK, Mo X, Palanichamy K, et al. Piperlongumine treatment inactivates peroxiredoxin 4, exacerbates endoplasmic reticulum stress, and preferentially kills high-grade glioma cells. Neuro Oncol 2014;16:1354–64.
34. Kim TH, Song J, Alcantara Llaguno SR, Murnan E, Liyanarachchi S, Palanichamy K, et al. Suppression of peroxiredoxin 4 in glioblastoma cells increases apoptosis and reduces tumor growth. PLoS One 2012;7:e42818.
35. Poschmann G, Grzendowski M, Stefanski A, Bruns E, Meyer HE, Stühler K. Redox proteomics reveal stress responsive proteins linking peroxiredoxin-1 status in glioma to chemosensitivity and oxidative stress. Biochim Biophys Acta 2015;1854:624–31.
36. Godbole S, Voß H, Gocke A, Schlumbohm S, Schumann Y, Peng B, et al. Multiomic profiling of medulloblastoma reveals subtype-specific targetable alterations at the proteome and N-glycan level. Nat Commun 2024;15:6237.
37. Nakashima R, Goto Y, Koyasu S, Kobayashi M, Morinibu A, Yoshimura M, et al. UCHL1-HIF-1 axis-mediated antioxidant property of cancer cells as a therapeutic target for radiosensitization. Sci Rep 2017;7:6879.
38. Bishop P, Rocca D, Henley JM. Ubiquitin C-terminal hydrolase L1 (UCH-L1): structure, distribution and roles in brain function and dysfunction. Biochem J 2016;473:2453–62.
39. Bilguvar K, Tyagi NK, Ozkara C, Tuysuz B, Bakircioglu M, Choi M, et al. Recessive loss of function of the neuronal ubiquitin hydrolase UCHL1 leads to early-onset progressive neurodegeneration. Proc Natl Acad Sci U S A 2013;110:3489–94.
40. Liu S, Gonzalez-Prieto R, Zhang M, Geurink PP, Kooij R, Iyengar PV, et al. Deubiquitinase activity profiling identifies UCHL1 as a candidate oncoprotein that promotes TGFbeta-Induced breast cancer metastasis. Clin Cancer Res 2020;26:1460–73.
41. O'Brien RJ, Xu D, Petralia RS, Steward O, Huganir RL, Worley P. Synaptic clustering of AMPA receptors by the extracellular immediate-early gene product Narp. Neuron 1999;23:309–23.
42. Liess AKL, Kucerova A, Schweimer K, Yu L, Roumeliotis TI, Diebold M, et al. Autoinhibition mechanism of the ubiquitin-conjugating enzyme UBE2S by autoubiquitination. Structure 2019;27:1195–210.e7.
43. Boles NC, Hirsch SE, Le S, Corneo B, Najm F, Minotti AP, et al. NPTX1 regulates neural lineage specification from human pluripotent stem cells. Cell Rep 2014;6:724–36.
44. Botlagunta M. Neuronal pentraxin 1 expression is regulated by hypoxia inducible factor-1α. Biochem Biophys Res Commun 2015;456:662–5.
45. Martinez-Chacin RC, Bodrug T, Bolhuis DL, Kedziora KM, Bonacci T, Ordureau A, et al. Ubiquitin chain-elongating enzyme UBE2S activates the RING E3 ligase APC/C for substrate priming. Nat Struct Mol Biol 2020;27:550–60.
46. Brown NG, VanderLinden R, Watson ER, Weissmann F, Ordureau A, Wu KP, et al. Dual RING E3 architectures regulate multiubiquitination and ubiquitin chain elongation by APC/C. Cell 2016;165:1440–53.
47. Liess AKL, Kucerova A, Schweimer K, Schlesinger D, Dybkov O, Urlaub H, et al. Dimerization regulates the human APC/C-associated ubiquitin-conjugating enzyme UBE2S. Sci Signal 2020;13:eaba8208.
48. Hu L, Cheng X, Binder Z, Han Z, Yin Y, O'Rourke DM, et al. Molecular and clinical characterization of UBE2S in glioma as a biomarker for poor prognosis and resistance to chemo-radiotherapy. Front Oncol 2021;11:640910.

49. Tang H, Fang T, Ji M, Wang JP, Song LL, Zhang QY, et al. UBE2S exerts oncogenic activities in urinary bladder cancer by ubiquitinating TSC1. Biochem Biophys Res Commun 2021;578:7–14.
50. Hu W, Li M, Chen Y, Gu X. UBE2S promotes the progression and olaparib resistance of ovarian cancer through Wnt/β-catenin signaling pathway. J Ovarian Res 2021;14:121.
51. Gui L, Zhang S, Xu Y, Zhang H, Zhu Y, Kong L. UBE2S promotes cell chemoresistance through PTEN-AKT signaling in hepatocellular carcinoma. Cell Death Discov 2021;7:357.
52. Luo Z, Xia M, Shi W, Zhao C, Wang J, Xin D, et al. Human fetal cerebellar cell atlas informs medulloblastoma origin and oncogenesis. Nature 2022;612:787–94.
53. Jay-Gerin JP. Ultra-high dose-rate (FLASH) radiotherapy: generation of early, transient, strongly acidic spikes in the irradiated tumor environment. Cancer Radiother 2020;24:332–4.
54. Lemon N, Canepa E, Ilies MA, Fossati S. Carbonic anhydrases as potential targets against neurovascular unit dysfunction in Alzheimer's disease and stroke. Front Aging Neurosci 2021;13:772278.